ADVANCED PHOTONICS RESEARCH Open Access
www.adpr-journal.com

Single Whispering Gallery Mode in Mesh-Structured Tubular Microcavity with Tunable Axial Confinement

*Yunqi Wang, Yang Wang, Gaoshan Huang, Ye Kong, Chang Liu, Zhe Zhao, Kaibo Wu, and Yongfeng Mei**

Single-mode lasing with high-beam quality and wide-range spectral purity is of fundamental importance in scientific and technical applications. Lacking a mode selection strategy, achieving single whispering gallery mode (WGM)-type lasing remains a challenge. Herein, a wide-range tunable single-WGM resonance in a mesh-structured tubular microcavity is realized by combining WGM resonance with distributed feedback effect, and the single mode can be systematically and precisely tuned by tailoring the geometry parameters of the hole array. In addition, switching between single mode and multimode WGM can be achieved at different axial directions of one individual tubular microcavity. The structure provides additional degrees of freedom to manipulate the resonant spectra characteristics and the spatial distribution of resonant modes, thus having a promising future in micro-/nano-optical devices.

1. Introduction

Optical microcavities, which can confine light effectively by resonant circulating, play an important role in light–matter interaction.[1] According to the differences in light confinement methods, optical microcavities can be classified as Fabry–Perot microcavities,[2–4] photonic crystal microcavities,[5,6] and whispering gallery mode (WGM) microcavities.[7,8] In a WGM microcavity, light propagates and circulates along the surface of the microcavity via total internal reflection, achieving high light intensity and energy density.[9] Due to the advantages of ultrahigh quality factor (Q factor) and small mode volume, WGM microcavities have attracted great interest in various fields, including sensors,[10–12] filters,[13,14] optical communications,[15] and especially, lasers.[16–21] In lasing applications, microcavities are utilized to decrease scattering loss and to improve light amplification. As for a laser, spectral width and threshold are the fundamental and significant parameters, which are tightly dependent on the Q factor of the microcavity and the mode volume (V) of the resonant mode.[22] The large Q/V value of WGM microcavities thus provides strong interaction between the active material and the microcavity interior, offering the possibility of obtaining lasers with low threshold and narrow linewidths.

Due to the advantages of high power, high-beam quality with Gaussian distribution, and relative wide-range spectral purity, single-mode lasing is of fundamental importance for scientific and technical applications.[23] Realizing single-mode resonance is necessary for sensing to improve the sensitivity and the spectral dynamic range. However, lacking of a mode selection strategy, WGM resonance is usually of a multimode nature, which limits the corresponding practical applications. To achieve single-mode WGM lasing, the straight-forward method is to minimize the cavity dimensions.[24,25] As the free spectral range (FSR) scales inversely with size, decreasing the cavity dimensions leads to an expanded FSR.[26] Single-mode WGM lasing can be obtained when only one resonant mode is left within the gain spectrum.[27] However, decreasing the cavity size corresponds to the increased curvature, leading to an evident scattering loss, which requires an increased lasing threshold.[28] Another common method used is based on size-matched coupled WGM microcavity.[29–33] Due to Vernier effect, the so-called photonics molecules can form an enlarged FSR, through which a tunable single-mode WGM can be obtained.[34] In the past decade, controlling the gain and loss through a parity-time (PT) symmetry system is considered as a novel approach for spectral modulation.[35,36] Some researchers have already obtained single-mode lasing in the PT symmetry-braking systems.[37,38] In addition, other approaches, e.g., metallic cavity-based light confinement,[39] spatially modulating the laser pump,[40,41] and using piezoelectric effect[42] are also believed to be able to achieve single-mode lasing. However, these methods are not experimentally compatible with all types of microresonators,[37] and most of the methods require design of complex micro-/nanostructures.[38]

In the case of tubular microcavities with the special geometrical feature,[43] additional degrees of freedom can be employed along the axial direction,[44,45] and therefore, strategies based on axial confinement along microtubes have been reported.

Y. Wang, Y. Wang, Prof. G. Huang, Y. Kong, C. Liu, Z. Zhao, K. Wu, Prof. Y. Mei
Department of Materials Science
Fudan University
Shanghai 200433, P. R. China
E-mail: yfm@fudan.edu.cn

The ORCID identification number(s) for the author(s) of this article can be found under https://doi.org/10.1002/adpr.202000163.

© 2021 The Authors. Advanced Photonics Research published by Wiley-VCH GmbH. This is an open access article under the terms of the Creative Commons Attribution License, which permits use, distribution and reproduction in any medium, provided the original work is properly cited.

DOI: 10.1002/adpr.202000163

Tian et al.[46] utilized origami-inspired technology to fabricate a diamond mesostructured microcavity with a discrete rotational symmetry, realizing a single WGM zero-phonon line emission with a high signal-to-noise ratio. However, with complex structure and delicate fabrication process, precise manipulation of the single-mode WGM microcavity has not been systematically demonstrated yet. In this work, we presented a wide-spectrum tunable single-mode WGM using a mesh-structured tubular microcavity with the mode selection ability, and the designed WGM microcavity generates so-called distributed feedback (DFB) effect in a relatively small volume. Through tailoring the period length and size of the hole arrays (i.e., mesh structure), the wavelength of single-mode WGM can be tuned on purpose. In addition, switching between single-mode and multimode WGM is experimentally achieved along the axis of one microtube. In comparison with other microcavities, the current modified microtubular structure provides additional degrees of freedom to manipulate the resonant spectra characteristics and the spatial distribution of modes, thus having a promising future in fundamental and practical applications in, for instance, lasing devices in miniaturized and integrated systems.

2. Theoretical Model

The photonic crystal-like structure with a missing row can generate single-mode emission due to DFB effect.[47–49] In a DFB microcavity, light travels throughout the periodic structure, scattering from each point along its path.[50] Due to the wavelength selectivity of Bragg effect, an interference-induced single-mode emission at a structure-dependent wavelength can be obtained.[50,51] However, traditional DFB lasers suffer from a relatively high lasing threshold and large mode volume. Imposing DFB effect on WGM with small volume could be a good option. **Figure 1**a thus shows the design idea of our structure. We found that, both theoretically and experimentally, by combining the tubular WGM microcavity with DFB structure, the electric field distribution of the resonant modes can be modulated and a desired single-mode WGM resonance can be obtained with appropriate structural design. As shown in our model (Figure 1b), the microcavity is designed with discrete periodic hole structure, which can generate DFB effect on intrinsic WGM-type resonance of a normal tubular microcavity, achieving the single-mode selection. The details of the model are clearly shown in Figure 1c–e. Figure 1c shows axial cross-sectional view of the microcavity, where periodic holes form the rotational symmetry of the structure. Here, the inner radius of the microtubular structure R_1 is set to be 5.4 μm while the outer radius R_2 is set to be 6.31 μm, and the structure is specifically characterized with a parameter, hole number M_0 (e.g., $M_0 = 11$ in this schematic). One may note that the thickness of the tube wall t is set to be a subwavelength value ($t = R_2 - R_1 = 0.91$ μm). In such circumstance, transverse magnetic (TM)-polarized WGM with electric field vector paralleled to z direction (axial direction) possesses much lower scattering loss and is preferentially considered in our simulation.[52] In addition, the subwavelength wall thickness also plays an important role in confining light propagation along radial direction, and thus only the fundamental radial mode is demonstrated.[46] Moreover, affected by the wavelength-scale axial barrier length, WGM is further restricted with the lowest axial mode index of 1.

To clearly demonstrate the DFB effect in the mesh-structured microcavity, the curvature of the tube structure is neglected, and thus DFB wavelength is able to be calculated using a planar geometry, as shown in Figure 1d. However, the wavelength-scale thickness of the tube wall should be considered to maintain the constant vacancy ratio (i.e., hole size h/period length a) at every vertical position along the radial direction, hole size h is supposed to increase with the height, causing the wedge-shape holes, as schematically shown in Figure 1e. For the sake of simplicity, we use the average value of the hole size (yellow dotted line) as a parameter in the following paragraphs. Due to the complexity of the mesh-structured microcavity, finite-difference time-domain (FDTD) method is adopted to solve the 3D Maxwell's equations, and typical characteristics of the resonant modes such as the resonance wavelength λ, Q factor, and electric field distribution can be obtained. Tuning of the single-mode

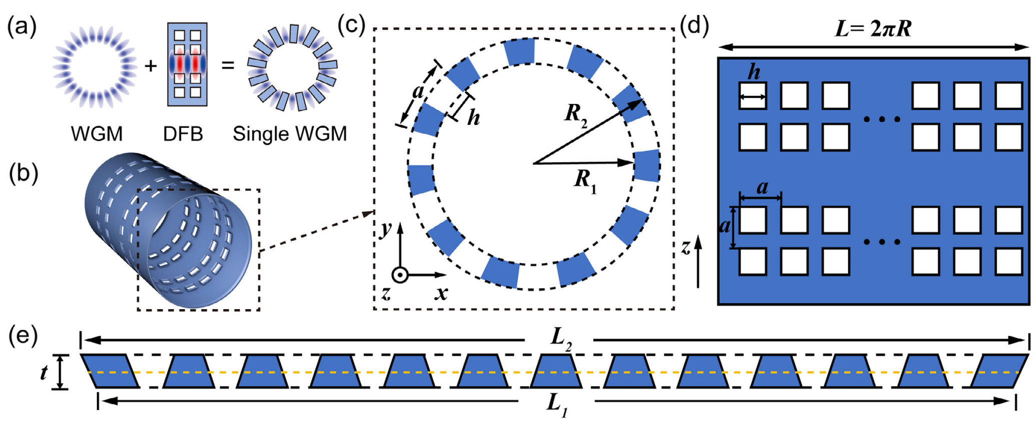

Figure 1. Schematic of the mesh-structured tubular microcavity. a) Illustration of the strategy to achieve a single WGM. b) 3D schematic of the microcavity. c) Axial cross-sectional view. R_1, R_2, a, and h represent inner radius, outer radius, period length, and hole size, respectively. d) Schematic of the planar DFB structure. The length of the structure is set as $L = 2\pi R$, where R is the curvature radius. e) Cross-sectional view of (d). The thickness t of the tube wall leads to wedge-shaped holes. Hole size h linearly increases along the radius, and the average hole size (marked by yellow dotted line) is chosen to characterize the structure.

© 2021 The Authors. Advanced Photonics Research published by Wiley-VCH GmbH

WGM in a pretty wide spectrum range is carried out through varying period length a and hole size h.

3. Realization of the Single WGM Resonance

Resonant spectra with varied period lengths a are shown in **Figure 2**a, where hole size h is fixed at 650 nm. Normal WGM is always measured as a series of modes with the similar intensity (Figure S1a, Supporting Information). However, spectra simulated with the current mesh-structured microcavity present obvious intensity difference, which proves the mode selection ability of the current cavity due to the interaction of WGM resonance and DFB effect. As for structure with period length $a = 1021$ nm (hole number $M_0 = 36$), the intensity of WGM with azimuthal number $m = 36$ is much higher than the adjacent modes (≈25 folds), indicating an effective mode suppression for unselected WGMs. Moreover, the spectrum presents a single-mode emission in spectral range of at least 400 nm (Figure S1b, Supporting Information), indicating a wide range mode selection. With a hole size h of 650 nm, single-mode emission of different azimuthal numbers can be achieved through tailoring the hole numbers M_0, indicating this mode-selection approach is structure dependent. Figure 2a shows that the increased M_0 causes a blue shift of the resonant wavelength. In addition, similar to normal WGM in microtube, the FSR of the resonance can be calculated by measuring the mode spacing in the spectrum, and the values are determined to be 32.22, 32.03, and 31.80 nm ($m = 34$–39) for $M_0 = 36$, 37, and 38, respectively. It is noted that FSR decreases with increasing M_0, and is smaller than that of microtubular cavity without mesh structure (35.24 nm, Figure S1c, Supporting Information). The phenomenon can be ascribed to the scattering loss caused by the introduction of additional holes, which leads to a decrease in effective refractive index n_{eff} (Figure S1d, Supporting Information). In this case, the lower effective refractive index generates decreased resonant wavelength and FSR.

It is worth noticing that the selected mode m and the hole number M_0 have a clear corresponding relationship, and only WGM with $m = M_0$ is selected, whereas other WGMs are suppressed. In addition, as shown in Figure 2b, WGMs with $m = M_0$ present a remarkably higher Q factor, which indicates less scattering loss and better light confinement.[53] In addition, compared with multimode WGM (microtubular cavity without mesh structure), Q factor of WGMs with $m = M_0$ is of the same level with that of multimode WGM, whereas Q factors of the other WGMs drop significantly. The selected WGM (i.e., $m = M_0$) with the largest intensity and the highest Q factor can be particularly explained by considering the distribution of electric field. As shown in Figure 2c, in the case of selected mode, the electric field distribution matches with the designed periodic mesh structure. The perfectly matched field distribution indicates the mode is well confined in the structure, and this can effectively reduce the possible scattering loss, showing a strong mode intensity. However, as for the suppressed mode ($m = 37$ for example), the electric field presents mismatched distribution (Figure 2d). Severe scattering loss in this case causes the decrease in resonant intensity, which is also reflected in the deterioration of Q factor. Quantitatively, the maximum intensity of mode with $m = 38$ is about 20 times larger than that of $m = 37$, whereas the minimum value of $m = 38$ mode is nearly one seventieth of that of $m = 37$. The distribution of electric field shown in Figure 2c,d prove that the selected mode should correspond a far better resonance. In other words, the periodic structure induces differences in field distribution, causing varying degrees of scattering loss. As a result, the structure-dependent single-mode selection can be achieved by changing the geometry of the mesh structure.

Figure 3a shows the simulated resonant spectra upon varying the hole size h from 650 to 700 nm. As shown in the figure, blue shift is observed with the increasing hole size h, indicating an effective method to manipulate the WGM resonant wavelength. Similar to the case of varying period length, the linear decrease in the wavelength can also be referred to the decrease in effective refractive index n_{eff} (Figure S2a, Supporting Information), in

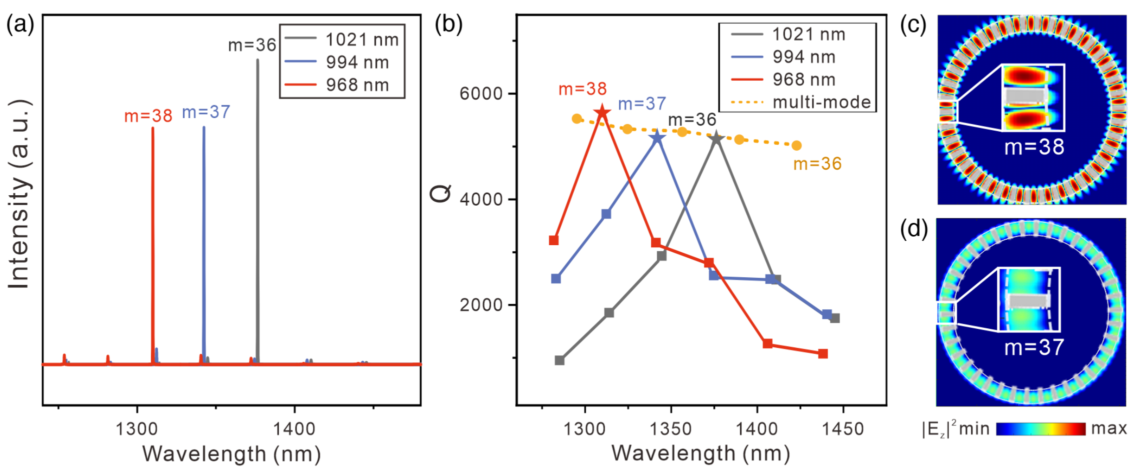

Figure 2. Mode selection with structures of different period lengths. a) Resonant spectra and b) Q factor simulated with period length a varying from 968 to 1021 nm. Simulated Q factor of multimode WGM (microtubular cavity without mesh structure) is shown in yellow dotted line. c) Color-coded distribution of z component of electric field ($|E_z|^2$) of mode with $m = 38$. d) Color-coded distribution of z component of electric field ($|E_z|^2$) of mode with $m = 37$. The intensities in (c) and (d) are normalized and shown in logarithmic scale, and the scale bar is presented at the bottom of (d).

© 2021 The Authors. Advanced Photonics Research published by Wiley-VCH GmbH

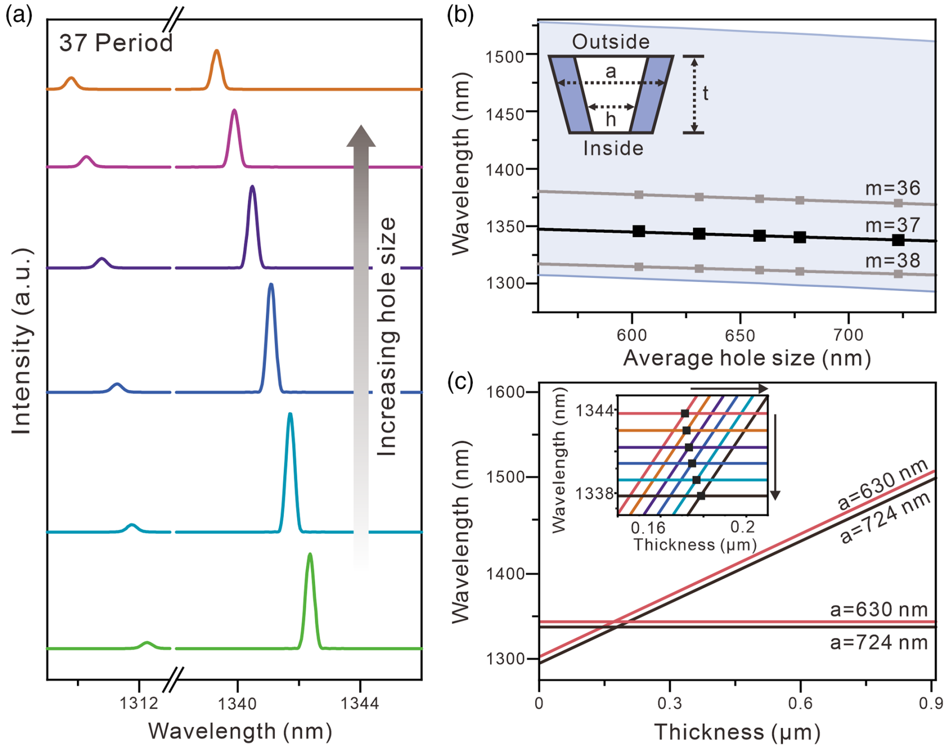

Figure 3. Mode selection with increasing hole size h. a) Resonant spectra simulated with varying hole size h from 650 to 700 nm (period length $a = 994$ nm). b) Resonant wavelength shifts with increasing hole size h. Corresponding DFB wavelength is shown with blue shadow. The lower blue line marks DFB resonant wavelength corresponding to the inner surface, and the upper blue line represents the DFB resonant wavelength at the outer surface. The inset is schematic of the wedge-shaped hole structure. c) Evolution of coupling wavelength along the radial direction. Sloping lines mark DFB wavelength shift, and horizontal lines indicate the WGM resonant wavelengths. Inset: the intersection points with hole sizes varying from 630 to 724 nm, with a step of 18.8 nm. The arrows show the increase in the hole size h. The curves corresponding to the same h are plotted with same color.

accordance with the formula: $\pi D n_{\text{eff}} = m\lambda$.[54] The black squares in Figure 3b correspondingly summarize the shift of modes with $m = 37$ as a function of hole size h. On the other hand, if DFB effect is considered (Figure S2b,c, Supporting Information), as Bragg's law $2an_{\text{d}} = q\lambda_0$ indicates, where $q = 2$ is the diffraction order, λ_0 is the DFB resonant wavelength, and n_{d} is the effective refractive index of the material, the wavelength should be linearly proportional to n_{d}, and thus increasing the hole size can lead to a decrease in the DFB resonant wavelength too.[55] Moreover, it is worth noting that the wedge-shaped hole (see also Figure 1e and the inset of Figure 3b) leads to a varied period along the vertical direction (e.g., from the inside to the outside surfaces), resulting in an evolution of DFB resonant wavelength. Therefore, the DFB resonant wavelength under a certain h cannot be treated as a single value but a range. The blue shadow area in Figure 3b shows the DFB resonant wavelength evolution while considering varied sizes and the wedge-shaped nature of the periodic holes at the same time. As the DFB resonant wavelength range is relatively large, a few modes of different azimuthal numbers seem to meet the wavelength-matching requirement. However, as mentioned earlier, only when the structure-matching condition $m = M_0$ is also satisfied can the mode selection approach be achieved. In this case, WGM with $m = 37$ in the 37-hole structure is selected, as shown in Figure 3b. To go into more details, Figure 3c shows the wavelength evolution with increasing thickness (i.e., from inner surface to outer surface of the tube wall). As n_{d} is designed to be constant along the radial direction because of the constant vacancy ratio, the DFB resonant wavelength increases linearly with increasing diameter. When DFB resonant wavelength equals to the WGM wavelength, the strong coupling can be expected and therefore it leads to effective mode selection. This phenomenon is further shown in Figure 3c with two typical hole sizes (630 and 724 nm). As shown, the corresponding intersection points locate in a very narrow range, indicating that the "coupling plane" is at an almost fixed position. A zoom-in view of the crossing area with varied hole sizes is shown in the inset of Figure 3c. With the increasing hole size h (see the arrows), both DFB and WGM resonant wavelengths present a blue shift, causing tiny shift of the intersection point. The possible explanation may be related to the evolution of the electric field distribution, larger hole size corresponds to smaller dielectric area and effective index, thus the scattering loss is aggravated and the mode may have a tendency to move outward.

4. Switching between Single-Mode and Multi-Mode WGM

To verify the conclusions derived from the simulation, the corresponding experiment was carried out with direct laser writing (DLW) technique and transmission spectra measurements. As shown in **Figure** 4a, based on two-photon absorption (TPA),

 © 2021 The Authors. Advanced Photonics Research published by Wiley-VCH GmbH

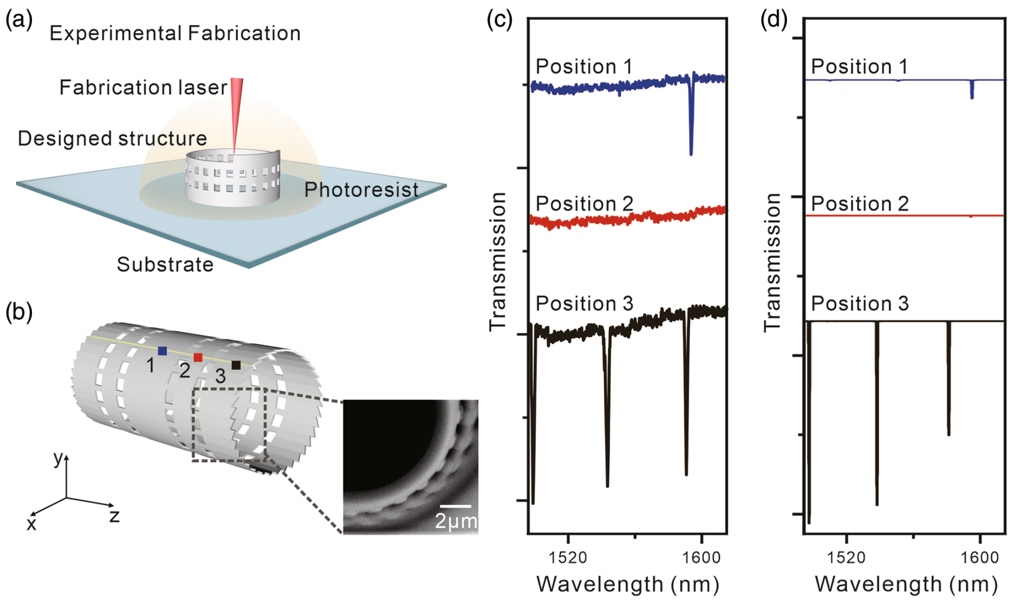

Figure 4. Resonant mode evolution along the axial direction. a) Schematic of the TPA-based DLW process. b) Schematic of the measured positions along the axial direction. In the axial direction (shown as a yellow line), three positions are measured and simulated, as marked by blue, red, and black squares, respectively. Inset: SEM image of the as-prepared sample. c) Measured transmission spectra and d) Simulated transmission spectra at different axial positions.

DLW serves as a novel method to fabricate complicated microstructures due to the high accuracy and design freedom.[56–59] In our work, structure corresponding to our theoretical model was successfully fabricated by a DLW approach, as shown in Figure 4b and S3, Supporting Information. As the surface quality plays an important role to its optical performance,[60] writing route was designed to be along the circumstance to ensure the surface smoothness (see Experimental Section for details).[56]

Figure 4c,d, respectively, shows the obtained transmission spectra and corresponding simulation. Three discrete locations along the axis of the microtube, including the center plane, the hole-array region, and the overhead region (see Figure 4b) were investigated. It is noticeable that spectra at varied axial positions present significant discrepancy. The obvious difference can be ascribed to the axial confinement diversity, verifying that the single WGM at the center plane (blue lines in Figure 4c,d) is obtained by the aforementioned mode selection from axial confinement. As have been illustrated earlier, WGMs at the center plane are supposed to be affected by the DFB effect, thus showing a single-mode feature. When the measured point is moved to the periodic hole-array region, no visible resonant signal is observed (red lines in Figure 4c,d). The possible explanation is attributed to the confinement of the mesh structure, where light suffers from server scattering loss due to the discontinuity characteristic of the structure. As a result, light can hardly propagate and none of the WGMs can be observed. The phenomenon is also proved by simulation results shown in Figure 4d. As the measured point continues to move to overhead region, normal WGM with a multimode nature is obtained (black lines in Figure 4c,d). A series of WGMs with an average FSR of ≈45 nm can be seen in the experimental spectrum, similar with the value derived from the simulation spectrum (41.5 nm). The discrepancy between the experimental value and the theoretical result can be attributed to the tiny size error between the design layout and the fabricated microtubular structure. One can see that the overhead region is far away from the hole-array region, which lead to the failure of mode selection due to the coupling between WGM and DFB resonant wavelengths. In other words, the mesh-structured tubular microcavities exhibit a confinement diversity along axial direction, and single-mode and multimode types of WGM resonances can be switched by changing the axial position.

5. Conclusion

In summary, we have demonstrated a tunable single WGM selection strategy. Combining the advantages of WGM resonance and DFB effect, the tubular mesh-structured microcavity with axial confinement can realize a wide-range mode selection at near infrared wavelengths. The desired wavelength of single-mode WGM is tuned by tailoring geometry of the periodic hole array, and thus the current mode selection approach is of great flexibility and precision. The numerical simulations are confirmed by the experimental result, and the switching between single-mode and multimode WGM was experimentally achieved along the axial direction. Our structure provides additional degrees of freedom to manipulate the resonant spectra and the spatial distribution of optical resonant modes, which should have a promising future in fundamental and practical applications.

6. Experimental Section

FDTD Simulation of the Mesh-Structured Microcavity: FDTD method was adopted to solve the 3D Maxwell's equations due to the complexity of the mesh-structured microcavity. Typically, a mesh-structured microcavity

 © 2021 The Authors. Advanced Photonics Research published by Wiley-VCH GmbH

with inner radius $R_1 = 5.4\,\mu m$, outer radius $R_2 = 6.31\,\mu m$ ($t = 0.91\,\mu m$), and axial length $L_a = 10\,\mu m$ was considered in the 3D simulation. The refractive index n of the tube was set to 1.48, which was the typical n value of the negative resist after polymerization (see in the following sections). Based on the perfect matched layers, reflection at the simulation domain boundary was absorbed. 1D detectors were placed at the center plane (at different positions along the axial direction in Figure 4d) in the tube wall to monitor the intensity change, and 2D detectors were used to obtain the electrical field distribution at resonant wavelengths. To get a clear picture of the DFB effect in the structure, 2D FDTD simulation was used to calculate DFB resonant wavelength with a simplified planar structure, and more details can be found in Supporting Information.

Fabrication of Mesh-Structured Microcavity: The Photonic Professional GT DLW system designed by Nanoscribe Company was applied to fabricate the supposed structure. A pulsed erbium-doped femto fiber laser centered at 780 nm with a repetition rate of 80 MHz and 100 femtoseconds pulse duration was used as the exposure source, which can polymerize the applied negative photoresist (Nanoscribe IP-L 780) through a polymerization process. To tightly focus the laser into the photoresist, an oil immersion lens (Leica, 100×, numerical aperture NA = 1.4) was used, then the resist at the focal spot of the laser was polymerized during exposure and further retained in the subsequent development process. The target structure was fabricated by scanning the laser beam throughout the resist guided with the 3D structure designed by Describe 2.1 software (Figure S3, Supporting Information). The fused glass substrate was cleaned with acetone and isopropanol (IPA). After further drying process, the substrate was dripped with a drop of resist on its center and fixed to the sample holder of the DLW system. After the laser writing of the structure, the sample was immersed into a propylene glycol methyl ether acetate solution for 30 min, followed by rinsing in a bath of IPA for 15 min to be freestanding. Piezoscanning mode and continuous mode with high precision was adopted in our experiment. To obtain the designed structure with high optical quality, the writing route was designed to be along the circumstance. In this way, writing trace was parallel to the light circling direction, and the desired surface smoothness can be achieved.

Morphological Characterizations: The morphological properties of the as-fabricated microcavities were characterized via scanning electron microscopy (SEM, JEOL JSM-6701F) and optical microscopy. Structural parameters of the obtained microtubular structure are as followed: inner radius $R_1 = 5.4\,\mu m$, outer radius $R_2 = 6.31\,\mu m$, thickness $t = 0.91\,\mu m$, axial length $L_a = 10\,\mu m$, hole number $M_0 = 31$, and hole size $h = 650$ nm.

Transmission Spectra Measurement: To obtain the optical characteristics of the structure, transmission spectra measurement at near infrared wavelengths (from 1500 to 1620 nm) were carried out through a coupling method. A single-mode, tunable external-cavity laser (Ando 4321D, linewidth 200 kHz) with a tapered optical fiber (waist diameter $\approx 1\,\mu m$) was utilized to evanescently excite the WGM coupling of the microtube cavity. The tapered optical fiber was homemade by heating and stretching a commercial single-mode fiber (Corning SMF-28e) with two stepper motor on both sides of the desired fiber waist. By vertically placing the tapered fiber near the microcavity with the 3D micropositioning system, some of the light can interact and couple with the microtube through its evanescent field. Using an indium gallium arsenide photoelectric detector (Thorlabs PDA10CS-EC), electrical signals converted by light left in the fiber was further monitored by a computer with a general-purpose interface bus data acquisition card (National Instruments). Therefore, through sweeping the wavelengths of the laser over a wide spectral range, light at certain wavelengths can couple into the microcavity and a series of discrete WGMs are observed as Lorentzian-shaped dips in the transmission spectrum.

Supporting Information

Supporting Information is available from the Wiley Online Library or from the author.

Acknowledgements

This work was supported by the National Natural Science Foundation of China (Nos. 51961145108 and 61975035) and the Science and Technology Commission of Shanghai Municipality (Nos. 20501130700, 19XD1400600, and 19JC1415500).

Conflict of Interest

The authors declare no conflict of interest.

Data Availability Statement

The data that support the findings of this study are available from the corresponding author upon reasonable request.

Keywords

distributed feedbacks, mode selections, single modes, tubular microcavities, whispering gallery modes

Received: November 28, 2020
Revised: January 16, 2021
Published online: March 14, 2021

[1] K. J. Vahala, *Nature* **2003**, *424*, 839.
[2] M. Pelton, C. Santori, J. Vuckovic, B. Y. Zhang, G. S. Solomon, J. Plant, Y. Yamamoto, *Phys. Rev. Lett.* **2002**, *89*, 054101.
[3] W. N. Du, S. Zhang, Q. Zhang, X. F. Liu, *Adv. Mater.* **2019**, *31*, 6.
[4] X. Q. Wu, Q. S. Chen, Y. P. Wang, X. T. Tan, X. D. Fan, *ACS Photonics* **2019**, *6*, 2470.
[5] O. Painter, R. K. Lee, A. Scherer, A. Yariv, J. D. O'Brien, P. D. Dapkus, I. Kim, *Science* **1999**, *284*, 1819.
[6] D. Bekele, Y. Yu, K. Yvind, J. Mork, *Laser Photonics Rev.* **2019**, *13*, 1970048.
[7] S. L. McCall, A. F. J. Levi, R. E. Slusher, S. J. Pearton, R. A. Logan, *Appl. Phys. Lett.* **1992**, *60*, 289.
[8] M. Sak, N. Taghipour, S. Delikanli, S. Shendre, I. Tanriover, S. Foroutan, Y. Gao, J. Yu, Y. Zhou, S. Yoo, C. Dang, H. V. Demir, *Adv. Funct. Mater.* **2020**, *30*, 1900054.
[9] D. K. Armani, T. J. Kippenberg, S. M. Spillane, K. J. Vahala, *Nature* **2003**, *421*, 925.
[10] M. R. Foreman, J. D. Swaim, F. Vollmer, *Adv. Opt. Photonics* **2015**, *7*, 168.
[11] F. Vollmer, S. Arnold, *Nat. Methods* **2008**, *5*, 591.
[12] Y. N. Zhang, N. S. Zhu, T. M. Zhou, Y. Zheng, P. P. Shum, *IEEE Sens. J.* **2020**, *20*, 833.
[13] F. Monifi, J. Friedlein, S. K. Oezdemir, L. Yang, *J. Lightwave Technol.* **2012**, *30*, 3306.
[14] A. A. Savchenkov, V. S. Ilchenko, A. B. Matsko, L. Maleki, *IEEE Photon. Technol. Lett* **2005**, *17*, 136.
[15] T. J. Kippenberg, J. Kalkman, A. Polman, K. J. Vahala, *Phys. Rev. A* **2006**, *74*, 051802.
[16] J. W. Wang, Y. Yin, Y. D. Yang, Q. Hao, M. Tang, X. X. Wang, C. N. Saggau, D. Karnaushenko, X. H. Yan, Y. Z. Huang, L. B. Ma, O. G. Schmidt, *ACS Photonics* **2019**, *6*, 2537.
[17] Y. C. Lv, X. Xiong, Y. Y. Liu, J. N. Yao, Y. J. Li, Y. S. Zhao, *Nano Lett.* **2019**, *19*, 1098.
[18] W. Zhang, J. N. Yao, Y. S. Zhao, *Acc. Chem. Res.* **2016**, *49*, 1691.

© 2021 The Authors. Advanced Photonics Research published by Wiley-VCH GmbH

[19] C. Wei, S. Y. Liu, C. L. Zou, Y. Y. Liu, J. N. Yao, Y. S. Zhao, *J. Am. Chem. Soc.* **2015**, *137*, 62.
[20] W. Noh, M. Dupre, A. Ndao, A. Kodigala, B. Kante, *ACS Photonics* **2019**, *6*, 389.
[21] L. Y. Zhao, Q. Y. Shang, Y. Gao, B. Jin, T. Y. Zhai, Q. Zhang, *J. Mater. Chem. C* **2019**, *7*, 12869.
[22] M. Pelton, J. Vuckovic, G. S. Solomon, A. Scherer, Y. Yamamoto, *IEEE J. Quantum Electron.* **2002**, *38*, 170.
[23] S. Suzuki, A. Schulzgen, N. Peyghambarian, *Opt. Lett.* **2008**, *33*, 351.
[24] M. Cai, O. Painter, K. J. Vahala, P. C. Sercel, *Opt. Lett.* **2000**, *25*, 1430.
[25] D. J. Gargas, M. C. Moore, A. Ni, S.-W. Chang, Z. Zhang, S.-L. Chuang, P. Yang, *ACS Nano* **2010**, *4*, 3270.
[26] X. Y. Lin, Y. F. Fang, L. J. Zhu, J. Zhang, G. S. Huang, J. Wang, Y. F. Mei, *Adv. Opt. Mater.* **2016**, *4*, 936.
[27] K. H. Li, Z. T. Ma, H. W. Choi, *Opt. Lett.* **2012**, *37*, 374.
[28] C. Y. Lu, S. W. Chang, S. L. Chuang, T. D. Germann, D. Bimberg, *Appl. Phys. Lett.* **2010**, *96*, 251101.
[29] H. D. Wan, L. Q. Liu, Z. Q. Ding, J. Wang, K. D. Lu, Z. X. Zhang, L. Zhang, *IEEE Photon. Technol. Lett.* **2017**, *29*, 2123.
[30] C. H. Zhang, C. L. Zou, H. Y. Dong, Y. L. Yan, J. N. Yao, Y. S. Zhao, *Sci. Adv.* **2017**, *3*, e1700225.
[31] C. Qiao, C. H. Zhang, Z. H. Zhou, H. Y. Dong, Y. X. Du, J. N. Yao, Y. S. Zhao, *Angew. Chem., Int. Ed.* **2020**, *59*, 15992.
[32] T. Grossmann, T. Wienhold, U. Bog, T. Beck, C. Friedmann, H. Kalt, T. Mappes, *Light Sci. Appl.* **2013**, *2*, e82.
[33] H. T. Wang, S. Liu, L. Chen, D. Y. Shen, X. Wu, *Sci. Rep.* **2016**, *6*, 20002.
[34] X. Wu, H. Li, L. Y. Liu, L. Xu, *Appl. Phys. Lett.* **2008**, *93*, 081105.
[35] K. G. Makris, R. El-Ganainy, D. N. Christodoulides, Z. H. Musslimani, *Phys. Rev. Lett.* **2008**, *100*, 103904.
[36] M. Liertzer, L. Ge, A. Cerjan, A. D. Stone, H. E. Tuereci, S. Rotter, *Phys. Rev. Lett.* **2012**, *108*, 173901.
[37] L. Feng, Z. J. Wong, R. M. Ma, Y. Wang, X. Zhang, *Science* **2014**, *346*, 972.
[38] H. Hodaei, M.-A. Miri, M. Heinrich, D. N. Christodoulides, M. Khajavikhan, *Science* **2014**, *346*, 975.
[39] M. Khajavikhan, A. Simic, M. Katz, J. H. Lee, B. Slutsky, A. Mizrahi, V. Lomakin, Y. Fainman, *Nature* **2012**, *482*, 204.
[40] F. X. Gu, F. M. Xie, X. Lin, S. Y. Linghu, W. Fang, H. P. Zeng, L. M. Tong, S. L. Zhuang, *Light Sci. Appl.* **2017**, *6*, e17061.
[41] Q. J. Lu, X. G. Chen, S. S. Xie, X. Wu, *Opt. Express* **2018**, *26*, 20183.
[42] J. F. Lu, Z. Yang, F. T. Li, M. M. Jiang, Y. F. Zhang, J. L. Sun, G. F. Hu, Q. Xu, C. X. Xu, C. F. Pan, Z. L. Wang, *Mater. Today* **2019**, *24*, 33.
[43] T. Kipp, H. Welsch, C. Strelow, C. Heyn, D. Heitmann, *Phys. Rev. Lett.* **2006**, *96*, 077403.
[44] D. O'Shea, C. Junge, M. Poellinger, A. Vogler, A. Rauschenbeutel, *Appl. Phys. B-Lasers Opt.* **2011**, *105*, 129.
[45] M. Ding, G. S. Murugan, G. Brambilla, M. N. Zervas, *Appl. Phys. Lett.* **2012**, *100*, 081108.
[46] Z. A. Tian, S. L. Li, S. Kiravittaya, B. R. Xu, S. W. Tang, H. L. Zhen, W. Lu, Y. F. Mei, *Nano Lett.* **2018**, *18*, 8035.
[47] O. Gauthier-Lafaye, D. Mulin, S. Bonnefont, X. Checoury, J. M. Lourtioz, A. Talneau, F. Lozes-Dupuy, *IEEE Photon. Technol. Lett.* **2005**, *17*, 1587.
[48] K. Inoue, H. Sasaki, K. Ishida, Y. Sugimoto, N. Ikeda, Y. Tanaka, S. Ohkouchi, Y. Nakamura, K. Asakawa, *Opt. Express* **2004**, *12*, 5502.
[49] A. Larrue, O. Bouchard, A. Moni-Nayrant, O. Gauthier-Lafaye, S. Bonnefont, A. Arnoult, P. Dubreuil, F. Lozes-Dlipuy, *IEEE Photon. Technol. Lett.* **2008**, *20*, 2120.
[50] H. Kogelnik, C. V. Shank, *J. Appl. Phys.* **1972**, *43*, 2327.
[51] A. Larrue, J. Campos, O. Gauthier-Lafaye, A. Monmayrant, S. Bonnefont, F. Lozes-Dupuy, *IEEE J. Sel. Top. Quant. Electron.* **2011**, *17*, 1236.
[52] G. S. Huang, V. A. B. Quinones, F. Ding, S. Kiravittaya, Y. F. Mei, O. G. Schmidt, *ACS Nano* **2010**, *4*, 3123.
[53] J. Ward, O. Benson, *Laser Photonics Rev.* **2011**, *5*, 553.
[54] M. C. Estevez, M. Alvarez, L. M. Lechuga, *Laser Photonics Rev.* **2012**, *6*, 463.
[55] Y. Wu, B. C. Yao, A. Q. Zhang, Y. J. Rao, Z. G. Wang, Y. Cheng, Y. Gong, W. L. Zhang, Y. F. Chen, K. S. Chiang, *Opt. Lett.* **2014**, *39*, 1235.
[56] Y. L. Li, Y. F. Fang, J. Wang, L. Wang, S. W. Tang, C. P. Jiang, L. R. Zheng, Y. F. Mei, *Lab Chip* **2016**, *16*, 4406.
[57] A. Selimis, V. Mironov, M. Farsari, *Microelectron. Eng.* **2015**, *132*, 83.
[58] A. Zhizhchenko, S. Syubaev, A. Berestennikov, A. V. Yulin, A. Porfirev, A. Pushkarev, I. Shishkin, K. Golokhvast, A. A. Bogdanov, A. A. Zakhidov, A. A. Kuchmizhak, Y. S. Kivshar, S. V. Makarov, *ACS Nano* **2019**, *13*, 4140.
[59] Z. L. Wu, Y. N. Qi, X. J. Yin, X. Yang, C. M. Chen, J. Y. Yu, J. C. Yu, Y. M. Lin, F. Hui, P. L. Liu, Y. X. Liang, Y. Zhang, M. S. Zhao, *Polymers* **2019**, *11*, 553.
[60] J. Y. Zhao, Y. L. Yan, Z. H. Gao, Y. X. Du, H. Y. Dong, J. N. Yao, Y. S. Zhao, *Nat. Commun.* **2019**, *10*, 870.

© 2021 The Authors. Advanced Photonics Research published by Wiley-VCH GmbH